

Learning Coordinate-based Convolutional Kernels for Continuous SE(3) Equivariant and Efficient Point Cloud Analysis

Jaemin Kim¹, Hee Bin Yoo^{2*}, Dong-Sig Han^{3*}, Byoung-Tak Zhang^{1,4}

¹Interdisciplinary Program in Neuroscience, Seoul National University

²Département d’Informatique, École Normale Supérieure (ENS)

³Department of Computing, Imperial College London

⁴Department of Computer Science and Engineering, Seoul National University

{jykim, btzhang}@bi.snu.ac.kr

Abstract

A symmetry on rigid motion is one of the salient factors in efficient learning of 3D point cloud problems. Group convolution has been a representative method to extract equivariant features, but its realizations have struggled to retain both rigorous symmetry and scalability simultaneously. We advocate utilizing the intertwiner framework to resolve this trade-off, but previous works on it, which did not achieve complete SE(3) symmetry or scalability to large-scale problems, necessitate a more advanced kernel architecture. We present *Equivariant Coordinate-based Kernel Convolution*, or *ECKConv*. It acquires SE(3) equivariance from the kernel domain defined in a double coset space, and its explicit kernel design using coordinate-based networks enhances its learning capability and memory efficiency. The experiments on diverse point cloud tasks, e.g., classification, pose registration, part segmentation, and large-scale semantic segmentation, validate the rigid equivariance, memory scalability, and outstanding performance of *ECKConv* compared to state-of-the-art equivariant methods.

1. Introduction

Modern deep learning on point clouds has been dominating various tasks and applications in the 3D vision domain [11, 16, 18]. Yet, it has often exploited the prior that an input is aligned to the canonical pose, deteriorating its feasibility to the real-world problems [11]. While training with data augmentation induces transformation robustness, many studies [2, 11, 14, 23] have shown that the reliance on augmentation is inefficient or underperforms compared to the model retaining symmetry in its architecture. Thus, designing pose-equivariant model has been a significant topic in

*The majority of the work for this publication was done while these authors were in Seoul National University.

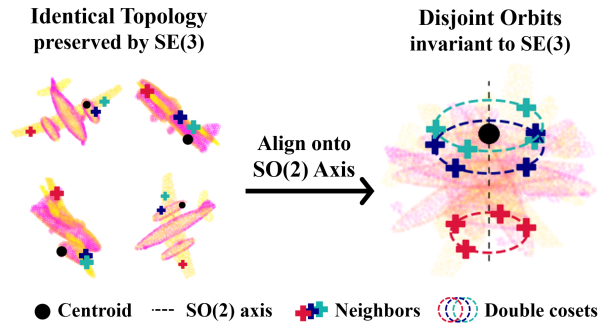


Figure 1. On the left, random SE(3) transformations are applied on the identical object point cloud. The black dots are centroids and colored plus signs designate neighbor points, where they are identical points with different poses. If these point clouds are transformed as the reference points are met on the subgroup, or the SO(2) axis, it is guaranteed that points with the identical topology lie on the disjoint orbit, or *double coset*, around the axis. Therefore, the SE(3) equivariant operation is achievable by utilizing the unique parameter defining those orbits. We visualized this concept with an example drawn from the ModelNet40 [42].

the 3D deep learning. Group convolution is one of the representative approaches to grant such symmetry, which derives the analogy from the translation equivariance of standard convolution towards the equivariance to group actions [5].

Group convolution on the 3D point clouds has the trade-off between the strict equivariance and model scalability [4, 49]. On the one hand, one can exploit a discrete group structure and directly expand kernel parameters to achieve scalability with restricted operations. However, it causes a discrepancy between the model and the continuity of groups, e.g., discretizing 3D rotations from a compact SO(3) space [12]. On the other hand, strict equivariance for continuous group spaces is guaranteed with the steerable convolution framework [6], which confines its features and kernels decomposable into the irreducible features and the

direct sum of maps between them [13, 35]. Such complex operations typically require expensive computational costs, restraining its applicability to large-scale 3D tasks.

One of the extended framework of group convolution, the *intertwiner* kernel convolution [7, 8], has been proposed to substitute the domain space from group to *quotient* space, which is more plausible to represent the operation over the physical space. Indeed, previous works based on this framework suggest more efficient discrete SE(3) equivariant convolution [49] or embed symmetry to continuous SO(3) actions [20] using *implicit kernel* [29, 30, 46]. However, a continuous SE(3) equivariant method has not been presented within the *intertwiner* framework, and their applications are not scalable enough to cover the large-scale 3D problems in the real-world.

This paper proposes Equivariant Coordinate-based Kernel Convolution (**ECKConv**), a continuous SE(3) equivariant convolutional network with scalability using *intertwiner* kernel framework. We configure the domain of kernel to embed SE(3) symmetry and parse the symmetric parameters from the normalized local neighbors using coordinate-based networks. With the *explicit kernel* design, the parsed information outputs linear maps equivariant to complete SE(3) with the enhanced local features and the scalability in terms of memory efficiency. Our method is verified through various translation/rotation invariant tasks and validates its symmetry on continuous rigid motions and practicality.

Our contributions are summarized as follows:

- We introduce **ECKConv** which adopts the *intertwiner* framework and computes the convolutional kernel from the parameters of a double coset space. It ensures a rigid symmetry against SE(3) from these parameters which corresponds to motion-invariant orbits as Figure 1.
- ECKConv extracts normalized double coset parameters from the local neighbors and computes the *explicit kernel* maps using coordinate-based networks. It develops an enhanced learning of local geometries and the scalability of our method. We prove the efficiency of explicit kernel with respect to the backpropagation.
- We verify the strict SE(3) equivariance and memory scalability of ECKConv through the classification and pose registration tasks in ModelNet40 [42]. The part segmentation in ShapeNet [3] and the semantic segmentation in S3DIS [1] also validate its advanced local feature learning and practicability to the large-scale problems.

2. Related Works

2.1. Deep Learning for 3D Point Cloud

PointNet [25] and PointNet++ [26] are early representative methods in point cloud deep learning. They introduce a weight-sharing MLP, *i.e.*, a one-dimensional convolution, to learn point features, and PointNet++ especially utilizes lo-

cal grouping and multi-scale (or resolution) mechanisms to enhance local geometry learning. Despite such techniques, they are ineffective in aggregating local features, relying on averaging or pooling among grouped points.

Convolution methods in point cloud learning retain the inductive bias of locality in every layer while coping with irregularly distributed samples in the cloud. Some early methods such as PointCNN [21] and PointConv [39] project distributed local features into regular features by learnable permutations or estimated density. KPConv [33] defines its kernel for irregular grid as the combination of weight bases, whose coefficients are gated by the distance between input and anchor coordinates. DGCNN [37] constructs a local cluster at each point by K-NN in the latent feature space, which aggregates point features independently to the distance in the coordinate space. It is also noteworthy that some studies adopt attention mechanisms and dynamically adjust the adjacency among point features [15, 40, 41, 45]. Yet, they are dependent on the data augmentations to induce symmetry to rigid motions only acting globally.

2.2. Group Equivariant Point Cloud Convolution

Group convolution is founded on either discrete group or steerable convolution, rooted from GCNN [5] and Steerable CNN [6]. TFN [35] decomposes the action of SO(3) and parametrizes the combination of equivariant bases to receive coordinate differences between points. Fuchs et al. [13] attach the attention mechanism among neighbors in TFN, where query and key are also the direct sum of learnable equivariant bases. As these steerable methods are not scalable to practical 3D vision problems, EPN [4] and E2PN [49] suggest discrete group methods based on KPConv [33], prescribing the assignment between discrete group or quotient space elements to replace the distance-based gate function. They show a capacity comparable to non-equivariant methods, but their symmetry is biased to the discretized rotations due to their attentive pooling over group dimensions. Recent studies have aimed to address both limitations in the previous works. CSEConv [20] suggests an implicit kernel invariant to continuous SO(3) by mapping double coset coordinates with learnable networks. Weijler and Hermosilla [38] propose a stochastic and efficient SE(3) convolution with lifted and sampled local coordinates. However, the symmetry of CSEConv is restricted to SO(3), and their performance in object-level analysis is limited compared to existing point cloud methods.

2.3. Equivariance outside Group Convolution

It is possible to implement symmetric networks outside the group convolution framework to avoid its trade-off. Some studies suggest model-agnostic frameworks that embed group equivariance into non-equivariant networks. For instance, Vector Neuron [9] suggests SO(3) equivari-

ant framework that augments a feature space into a bundle of 3D vectors. Frame Averaging [24] proposes a theoretical framework that approximate integration over group into averaging over equivariant *frame*, the finite subset of the group. Kaba et al. [19] and Mondal et al. [22] introduce to canonicalize the input orientation via additional equivariant networks. Although they retain the capacity of their foundation networks, they have limited symmetry to global SO(3) actions [9], or require high computational costs, pretrained networks [19], or the prior to the input orientation [22].

Meanwhile, there are studies that extract rotation invariant coordinate representations among point cloud clusters [32, 43, 44]. They have a similarity to ours in utilizing information invariant to rigid transformations during the operation. However, their heuristic design and selection of such information make these methods susceptible to local references [43], utilize ambiguous representations to a certain situation [44], or rely on the assumption that global transformation is equally applied to every local region [32]. These limitations necessitate the study that addresses the trade-off by the group convolution within its field.

3. Group Equivariant Convolution Framework using Intertwiner Kernel

This section outlines the mathematical framework and the motivation of our architectural design. We refer the readers to the previous works [7, 8, 20, 49] for a better understanding of detailed derivations. A group convolution is naturally derived from the standard convolution, simply substituting its symmetry against shifts into inverse actions closed on the group space [5, 8]:

$$(f * \kappa)(g) = \int_G \kappa(g^{-1}h)f(h)dh, \quad (1)$$

where f is an input feature, κ is a kernel, and g is a coordinate of point in the group space. This expression is sufficient for modelling the equivariance to discrete groups. However, real-world problems often require the symmetry to continuous groups, and a naive integration on continuous group space is computationally intractable for data acquired from a physical space.

Cohen et al. [7, 8] propose the framework that models the group equivariant convolution as a general linear map between fields by introducing the intertwiner $\text{Hom}(V_1, V_2)$ to the kernel function. V_1 and V_2 are fields of the input and output feature spaces, whose coordinates are from a homogeneous space. Notably, the convolution over group can be replaced into the equivalent operation over a quotient space, such as a 3D sphere, with $\kappa : G/H_1 \rightarrow \text{Hom}(V_1, V_2)$:

$$(f * \kappa)(x) = \int_{G/H_1} \kappa(s_2(x)^{-1}y)\rho_1(h_1(y, s_2(x)^{-1}))f(y)dy, \quad (2)$$

where $\rho_1 : G \rightarrow \text{GL}(V_1)$ is a representation, $s_2 : G/H_2 \rightarrow G$ is a section map for group G and subgroup H_2 , and $h_1(x, g) = s_1(gx)^{-1}gs_1(x)$ for $g \in G$, a section map s_1 for subgroup H_1 , and $x \in G/H_1$. For convenience, when $G = \text{SO}(3)$ and $H_2 = \text{SO}(2)$, assume that $s_2(x)^{-1}$ transforms x to the reference of H_2 , e.g., the north pole. The constraint on kernel $\kappa(\cdot)$ is required to retain the equivariance over group G as Equation (3), where the kernel preserves the symmetry to actions of subgroup H_2 :

$$\kappa(hy) = \rho_2(h)\kappa(y)\rho_1(h_1(y, h)^{-1}), \quad h \in H_2. \quad (3)$$

Cohen et al. [7, 8] also derive that $\kappa(\cdot)$ with Equation (3) has an equivalent function whose domain is in double coset space, where double cosets are disjoint bundles of quotient space elements transitive to H_2 actions. To concretize G -equivariant operation, previous works [20, 49] specify some configurations that $H_1 = H_2 = \text{SO}(2)$ and $\rho_1 = \rho_2 = \text{id}$, assuming that V_1 and V_2 are invariant. Consequently, the kernel function becomes an unconstrained function as:

$$(f * \kappa)(x) = \int_{G/H_1} \kappa(s_2(x)^{-1}y)f(y)dy, \quad (4)$$

s.t. $\kappa : H_2 \backslash G/H_1 \rightarrow \text{Hom}(V_1, V_2)$,

where the map from quotient space to double coset space is omitted with an abuse of notation. Those previous methods, however, simplified the operation to the integration on the discretized $\text{SE}(3)/\text{SO}(2)$ quotient space [49] or confined symmetry to continuous $\text{SO}(3)$ [20].

4. Method

This section delineates the methodology of ECKConv. First, we briefly mention how the domain of kernel is defined for the $\text{SE}(3)$ equivariance of convolution. Then, we explain how the explicit kernel architecture computes our kernel value from double cosets using coordinate-based networks with the theoretical analysis on its scalability. Finally, we suggest the convolution block and its residual architecture for solving the point cloud problems.

4.1. Continuous SE(3) Equivariant Convolution

ECKConv expands the double coset space (4) equipped with rotation and translation symmetry by configuring G into $\text{SE}(3) = \text{SO}(3) \times \mathbb{R}^3$. We adopt the derivation by Zhu et al. [49]; an element g in the double coset space is expressible as the pair of ZYZ Euler angles and translation when $G = \text{SE}(3)$ and $H_1 = H_2 = \text{SO}(2)$. Let us denote that $g \equiv (R_z(\alpha_g)R_y(\beta_g)R_z(\gamma_g), [x_g, y_g, z_g]) \in G$, $h_1 = R_z(\gamma_{h_1}) \in H_1$, and $h_2 = R_z(\gamma_{h_2}) \in H_2$. Then, we can write a double coset element g as follows:

$$H_2gH_1 = \left\{ (R_z(\alpha_g + \gamma_{h_2})R_y(\beta_g)R_z(\gamma_g + \gamma_{h_1}), R_z(\gamma_{h_2} + \gamma_t)[r_g, 0, z_g]^\top) \mid \forall h_1, h_2 \in \text{SO}(2) \right\}, \quad (5)$$

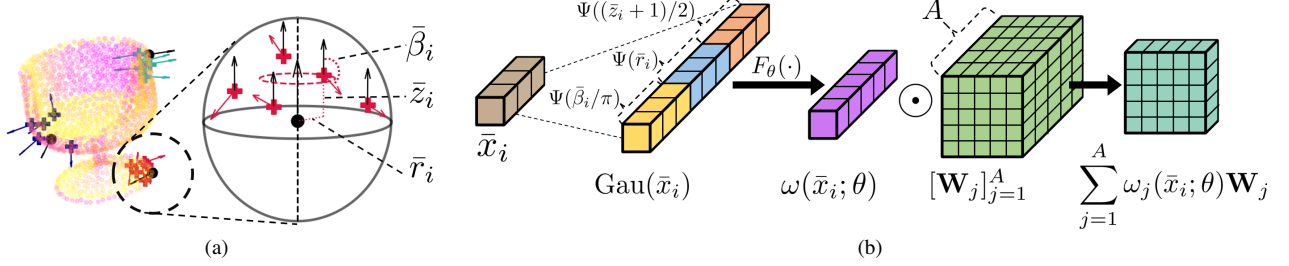


Figure 2. The implementation details in ECKConv. (a) The neighbor points within a radius r around each centroid are sub-sampled by ball query [26]. After they are aligned by the inverse of section map as Equation (6), $\bar{\beta}_i$, \bar{r}_i , and \bar{z}_i , which correspond to the double coset parameters, are acquirable as depicted. These neighbor points are actually computed from the ModelNet40 [42] object with normal vectors. (b) The computation of explicit kernel in ECKConv. First, it maps a double coset parameter $\bar{x}_i = [\bar{\beta}_i, \bar{r}_i, \bar{z}_i]$ into Gaussian embedding $[\Psi(\bar{\beta}_i/\pi), \Psi(\bar{r}_i), \Psi(\bar{z}_i/2)]$ [47, 48]. Then the embedding is projected by F_θ to $\omega(\bar{x}_i; \theta)$, a coefficient vector with the dimension A . The kernel value of $\kappa(\cdot)$ is gained from the weighted summation of learnable bases $[\mathbf{W}_j]_{j=1}^A$ by $\omega(\bar{x}_i; \theta)$, i.e., $\sum_{j=1}^A \omega_j(\bar{x}_i; \theta) \mathbf{W}_j$.

where $\gamma_t = \text{atan2}(y_g, x_g)$ and $r_g = \sqrt{x_g^2 + y_g^2}$ denote displacements. These notations are useful since the whole set grouped by Z-axis rotations from $\text{SO}(2)$ is an element of double coset. To summarize, a double coset element in $\text{SO}(2) \backslash \text{SE}(3) / \text{SO}(2)$ are uniquely representable as $[\beta_g, r_g, z_g]$, and the convolution equivariant to continuous $\text{SE}(3)$ can be built with the kernel depends on them.

4.2. Implementations of ECKConv

We realize the framework in Section 4.1 actually equivariant to continuous $\text{SE}(3)$ actions unlike the previous work symmetric to discrete $\text{SE}(3)$ [49]. Let us suppose the locality assumption and the integration approximation rule from Kim et al. [20]. Then, the formulation of ECKConv is written as follows:

$$\begin{aligned} (f * \kappa)(x) &= \sum_{x_i \in \mathcal{N}(x)} \kappa(s(x)^{-1}x_i) f(x_i), \\ \text{s.t. } \kappa : \text{SE}(3)/\text{SO}(2) &\rightarrow \mathbb{R}^{C_{\text{out}} \times C_{\text{in}}}, \\ f : \text{SE}(3)/\text{SO}(2) &\rightarrow \mathbb{R}^{C_{\text{in}} \times 1}, \end{aligned} \quad (6)$$

where $s : \text{SE}(3)/\text{SO}(2) \rightarrow \text{SE}(3)$ is a section map. The domain space of Equation (6) is factorizable into $\mathbb{R}^3 \times S^2$ since $\text{SE}(3) = \text{SO}(3) \times \mathbb{R}^3$ and $\text{SO}(3)/\text{SO}(2) \equiv S^2$. The coordinates of point clouds naturally represent \mathbb{R}^3 . The S^2 space is manifestible with any representations equivariant to $\text{SE}(3)$ that map 3D coordinates to unit vectors. For instance, we can use either the surface normal vectors or heuristic augmentation as Algorithm 1 in the supplementary material.

4.2.1. Local Neighboring and Double Coset Encoding

As we augment the domain into $\mathbb{R}^3 \times S^2$, let us assume a point cloud is composed of tuples of coordinate and normal vector (\mathbf{x}, \mathbf{n}) . Then, the local neighborhood, i.e., the region where we integrate, is determined by a ball query [26], which is defined as $\mathcal{N}((\mathbf{x}, \mathbf{n}); r, k) = \{(\mathbf{x}_i, \mathbf{n}_i) \in \mathcal{P} \mid \|\mathbf{x} - \mathbf{x}_i\|_2 \leq r, i = 1, \dots, k\}$, where r is a radius and k is the

maximal number of samples in ball query algorithm. It is a well-established approach that helps utilize the geometry of input points in the Euclidean space and normalize the scale of receptive field by convolution, suggested by many previous works with the locality assumption [4, 26, 33, 49].

We encode the double coset parameters $[\bar{\beta}_i, \bar{r}_i, \bar{z}_i]$ of each neighbor point $x_i = (\mathbf{x}_i, \mathbf{n}_i)$ referring to the local coordinate system of ball query centroid $x = (\mathbf{x}, \mathbf{n})$. These parameters correspond to $[\beta_g, r_g, z_g]$ of $s(x)^{-1}x_i$ from Equations (5) and (6) and are acquired as follows:

$$\begin{aligned} \bar{x}_i &= [\bar{\beta}_i, \bar{r}_i, \bar{z}_i], \quad \text{s.t. } \bar{\beta}_i = \arccos(\mathbf{n}^\top \cdot \mathbf{n}_i), \\ \bar{z}_i &= (\mathbf{n}^\top \cdot \frac{\Delta_i}{\|\Delta_i\|}) \cdot \|\Delta_i\|/r, \\ \bar{r}_i &= \sqrt{1 - (\mathbf{n}^\top \cdot \frac{\Delta_i}{\|\Delta_i\|})^2} \cdot \|\Delta_i\|/r, \end{aligned} \quad (7)$$

where $\Delta_i = \mathbf{x}_i - \mathbf{x}$ and r is a ball query radius. The geometric interpretation of Equation (7) is in Figure 2a, where the local coordinate system by x is aligned to a zero-centered Z-axis and $\text{SE}(3)$ invariant information of x_i is encoded to \bar{x}_i . Thus, the operation only processes the double coset parameters in the scale-normalized region and enables each ECKConv layer to learn $\text{SE}(3)$ -equivariant local geometries.

4.2.2. Explicit Kernel using Coordinate-based Networks

An explicit kernel function $\kappa(\cdot)$ consists of the combination of learnable linear maps as Equation (8), inspired by various convolution methods that compute the integration over irregular samples [4, 33, 34, 49].

$$\kappa(s(x)^{-1}x_i; \theta, [\mathbf{W}_j]_{j=1}^A) = \sum_{j=1}^A \omega_j(\bar{x}_i; \theta) \mathbf{W}_j, \quad (8)$$

$$\text{s.t. } s(x)^{-1}x_i \in \mathbb{R}^3 \times S^2, \bar{x}_i \in \text{SO}(2) \backslash \text{SE}(3) / \text{SO}(2),$$

where input $s(x)^{-1}x_i$ from the quotient space is mapped to the double coset \bar{x}_i by Equation (7), $\mathbf{W}_j \in \mathbb{R}^{C_{\text{out}} \times C_{\text{in}}}$, and A

is the number of anchor bases. Previous studies determine the values of gate functions $\omega_j(\cdot)$ by the distance between input coordinates and anchor points in the 3D space. However, they do not fit in our kernel function, as it is obscure to measure the distance in the double coset space.

Instead, we incorporate the coordinate-based networks to surrogate the metric over the double coset space inspired by CSEConv [20]. Neural networks $F_\theta(\cdot)$ map coordinates \bar{x}_i into unbounded coefficients ω_j for each anchor basis as:

$$\begin{aligned} \omega(\bar{x}_i; \theta) &= [\omega_j]_{j=1}^A = F_\theta(\text{Gau}(\bar{x}_i)) \in \mathbb{R}^A, \\ \text{s.t. } \text{Gau}([\bar{\beta}_i, \bar{r}_i, \bar{z}_i]) &= [\Psi(\bar{\beta}_i/\pi), \Psi(\bar{r}_i), \Psi((\bar{z}_i+1)/2)], \quad (9) \\ \Psi(x) &= [\psi(x, 0), \psi(x, 1/d), \dots, \psi(x, (d-1)/d)], \end{aligned}$$

where $\psi(x, y) = \exp(- (x-y)^2/2\sigma^2)$ is a Gaussian kernel with $\sigma = 0.05$ and $\text{Gau}(\cdot) \in \mathbb{R}^{3d}$ is referred to as Gaussian embedding [47, 48]. By mapping $[\bar{\beta}_i, \bar{r}_i, \bar{z}_i]$ into a range $[0, 1]$, Zheng et al. [47, 48] showed that Gaussian embedding provides the balance between memorization and generalization of coordinate learning with its bounded rank. Then, combining Equations (6) and (8) is written as:

$$(f * \kappa)(x) = \sum_{x_i \in \mathcal{N}(x)} \left(\sum_{j=1}^A \omega_j(\bar{x}_i; \theta) \mathbf{W}_j \right) f(x_i). \quad (10)$$

This might be interpretable as an implicit kernel since $\omega(\cdot)$ is a coordinate-based networks. However, we separate $\omega(\cdot)$ and basis maps \mathbf{W}_j as an explicit kernel, and reorder Equation (10) as follows inspired by Wu et al. [39]:

$$(f * \kappa)(x) = \sum_{j=1}^A \mathbf{W}_j \sum_{x_i \in \mathcal{N}(x)} \omega_j(\bar{x}_i; \theta) f(x_i), \quad (11)$$

which is the final formulation of ECKConv.

4.3. Scalability Improvement in ECKConv

Now we show the significance of this modification with respect to the computational benefit of Equation (11), although the operations in Equations (10) and (11) are equivalent [39], through the following proposition.

Proposition 4.1. *Let C_{in} be the dimension of input feature, C_{out} be the dimension of output feature, K be the cardinality of neighbors, and A be the cardinality of anchor bases. Then the cost from the derivative by θ , which is the parameter of ω , reduces from $\mathcal{O}(AKC_{in}C_{out})$ to $\mathcal{O}(A(KC_{in} + C_{in}C_{out}))$.*

Proof. Let us denote $Y = (f * \kappa)(x) \in \mathbb{R}^{C_{out}}$. Since the modification does not influence $\omega(x)$, the computation cost of $\nabla_\theta \omega$ is constant. Then one can distinguish the formulas

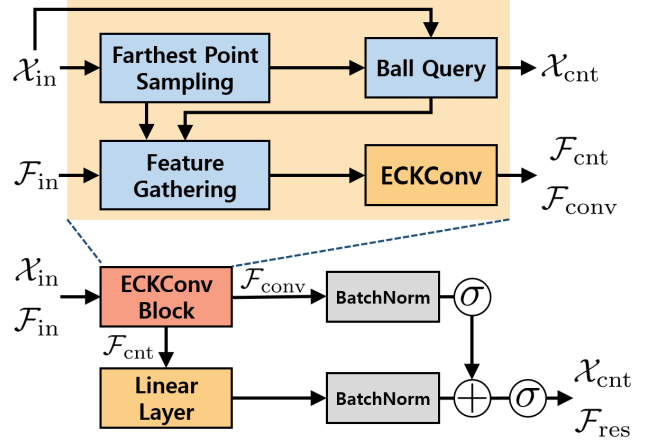


Figure 3. Architectures of ECKConv and its residual connection. We apply batch normalizations and activations (σ) in the order shown in the figure. As we only visualize abstract flow of the ECKConv block and its residual block, please refer to Section 7.1 in the supplementary material for more details.

of $\nabla_{\omega_j} Y$ according to the operations as follows:

$$\nabla_{\omega_j} Y = \begin{cases} \sum_{i=1}^K \mathbf{W}_j f(x_i) & \text{from Equation (10),} \\ \mathbf{W}_j \sum_{i=1}^K f(x_i) & \text{from Equation (11).} \end{cases} \quad (12)$$

The cost by the summation of products between \mathbf{W}_j and $f(x_i)$ is $\mathcal{O}(K C_{in} C_{out})$, and the cost by the product between \mathbf{W}_j and the summation of $f(x_i)$ s is $\mathcal{O}(K C_{in} + C_{in} C_{out})$. Since $\nabla_\theta Y = [\nabla_{\omega_j} Y]_{j=1}^A \nabla_\theta \omega$, the cost by $\nabla_\theta Y$ alters from $\mathcal{O}(AK C_{in} C_{out})$ to $\mathcal{O}(A(K C_{in} + C_{in} C_{out}))$. \square

Proposition 4.1 states that Equation (11) is equivalent to Equation (10) with reduced memory cost during the back-propagation. Considering the equivalence of Equation (10) to the implicit kernel, such as CSEConv [20], it necessitates the explicit kernel for the scalability, enabling more parameters on each layer and deeper network architecture.

4.4. Architecture of ECKConv Block and Residuals

The preceding components coalesce into a single block of ECKConv as Figure 3. We denote the input with N points as $(\mathcal{X}_{in}, \mathcal{F}_{in})$ where $\mathcal{X}_{in} = \{x^n | x^n = (\mathbf{x}^n, \mathbf{n}^n)\}_{n=1}^N$, $\mathcal{F}_{in} = \{f^n | f^n = f(x^n)\}_{n=1}^N$, and $\mathbf{x}^n, \mathbf{n}^n$, and f^n are the coordinate, normal vector, and feature of n th point. A farthest point sampling [26] chooses centroid points \mathcal{X}_{cnt} and the block gathers features \mathcal{F}_{cnt} that correspond to these centroids. After a ball query finds neighbor points $\mathcal{N}(x^n)$ for each centroid x^n and their corresponding features are also gathered, the ECKConv operates the convolution in Equation (11) and outputs \mathcal{F}_{conv} . The pair of $(\mathcal{X}_{cnt}, \mathcal{F}_{conv})$ becomes an output point cloud of the ECKConv block.

Furthermore, we implement the residual connection block [17] of ECKConv for the enhanced model capability as Figure 3, inspired by previous point convolution methods [33, 49]. The features of centroids \mathcal{F}_{cnt} are propagated by a linear layer, summed with $\mathcal{F}_{\text{conv}}$, and become new output features \mathcal{F}_{res} paired with \mathcal{X}_{cnt} .

5. Experiments

We conducted classification and pose registration task in the ModelNet40 [42] to verify the memory scalability, enhanced model capability, and rigorous SE(3) equivariance of ECKConv. Then it is validated on more complex tasks, *i.e.*, object part and indoor semantic segmentation, to verify its understanding of local geometries with equivariance and scalability to the real world. Please refer to the supplementary material for detailed training configurations.

Classification: It is the most standard task where a model classifies an input point cloud to one of 40 object categories. As in previous studies [20, 49], we trained and evaluated models with or without applying SO(3) rotations, meaning 4 cases were reported for each model.

Pose Registration: In this task, a model predicts the relative SE(3) transformation between two identical objects with different poses. We measured the relative angle error and translation RMSE between the estimated and ground truth transformations for assessment.

Object Part Segmentation: ShapeNet [3] contains objects over 16 categories, and point samples of the object are annotated with 50 part segmentation labels defined disjointly by their object category. A model outputs part segmentation labels classifiable into 50 categories per every sample point, given the whole point cloud and its object label. The segmentation performances were measured with mIoUs averaged over instances or part classes.

Indoor Semantic Segmentation: We conducted a semantic segmentation using the S3DIS [1] that contains indoor scenes sampled from real-world environments. This benchmark is challenging due to its enormous scale, where point clouds are densely sampled from 271 rooms across 6 different areas covering over $6000m^2$ and labeled with one of 13 semantic classes. We used Area 5 as the test set and trained with the rest of Areas following previous works [32–34].

5.1. Classification and Scalability Evaluation

We prepared two variations of our classification models: they either used the true normal vector or Algorithm 1 as the S^2 input (**ECKConv-Normal** and **ECKConv**). Baselines were categorized into three types: the non-equivariant methods [15, 26, 33, 37, 39, 41], the model-agnostic methods [9, 19, 22, 24] based on DGCNN [37], and the group convolution methods [4, 13, 20, 35, 49] including both discrete and steerable methods. Furthermore, we experimented **ECKConv-mini** which has identical model setups, *e.g.*, the

Table 1. Classification accuracy on the ModelNet40 dataset. Since PRLC [22] requires the prior that input has an aligned orientation, it is impossible to apply SO(3) augmentation during its training. † denotes the results reported from previous works [20, 49].

| Models | Classification Accuracy (%) | | | |
|------------------|-----------------------------|--------------|--------------|--------------|
| | I/I | I/SO(3) | SO(3)/I | SO(3)/SO(3) |
| PointNet++ [26]† | 89.13 | 9.58 | 81.16 | 80.29 |
| PointConv [39] | 92.31 | 5.29 | 88.14 | 87.74 |
| KPConv [33]† | 91.25 | 14.56 | 84.84 | 83.39 |
| DGCNN [37] | 91.41 | 14.34 | 88.24 | 87.97 |
| PCT [15]† | 91.25 | 15.84 | 86.39 | 84.20 |
| PTv3 [41] | 92.54 | 13.65 | 86.91 | 88.17 |
| VN [9] | 90.52 | 90.52 | 90.40 | 90.28 |
| FA [24]† | 82.25 | 82.25 | 82.01 | 82.01 |
| LC [19] | 88.33 | 88.87 | 88.09 | 88.12 |
| PRLC [22] | 88.49 | 88.45 | - | - |
| TFN [35]† | 62.28 | 62.28 | 62.64 | 62.64 |
| SE(3)-T [13]† | 71.60 | 71.60 | 73.01 | 73.01 |
| EPN [4]† | 91.45 | 31.08 | 86.60 | 86.60 |
| E2PN [49]† | 91.58 | 44.47 | 89.47 | 88.58 |
| CSEConv [20]† | 83.79 | 83.75 | 83.83 | 83.75 |
| ECKConv-mini | 87.40 | 87.40 | 87.32 | 87.36 |
| ECKConv | 90.52 | 90.52 | 90.19 | 90.19 |
| ECKConv-Normal | 91.37 | 91.37 | 90.92 | 90.92 |

Table 2. Cost table of the equivariant classification baselines.

| Models (Batch Size = 12) | Memory (GB) ↓ | | #Batch/sec ↑ | | #params |
|-----------------------------|---------------|-------------|--------------|--------------|---------|
| | Train | Eval | Train | Eval | |
| VN [9] | 6.10 | 1.98 | 4.34 | 8.70 | 2.9M |
| EPN [4] | 13.40 | 6.34 | 2.11 | 3.36 | 3.2M |
| E2PN [49] | 3.94 | 2.41 | 8.94 | 18.97 | 2.7M |
| ECKConv | <u>4.89</u> | 1.28 | <u>7.74</u> | <u>15.09</u> | 27.7M |
| CSEConv [20] | 2.95 | 0.44 | 30.71 | 59.77 | 2.1M |
| ECKConv-mini | 0.72 | 0.28 | 23.13 | 42.74 | 1.9M |

number of layers, layer-wise input/output dimensions, and the size of neighbors, to CSEConv [20] for the fair scalability comparison and substantiation of Proposition 4.1.

Table 1 shows that ECKConv-Normal reached the best accuracy over 91% when either the training or test set were rotated. Even without the normal vector input, ECKConv reached comparable accuracy to Vector Neurons [9] which is only equivariant to SO(3), and ECKConv-mini achieved nearly 4%p higher accuracy than CSEConv. These results validate the performance benefit of ECKConv against relying on augmentation and previous equivariant methods.

We measured the efficiency of equivariant baselines and ECKConv variants in Table 2. While ECKConv maintained an efficiency comparable to E2PN, the comparison between CSEConv and ECKConv-mini revealed the benefit of explicit kernel in terms of memory as stated in Proposition 4.1. In conclusion, ECKConv demonstrates its scalability regarding both model capacity and memory efficiency.

Table 3. Pose registration results on the ModelNet40. We reproduced the methods by Chen et al. [4] and Zhu et al. [49] for KPConv, EPN, and E2PN, which do not estimate the translation difference. Models were evaluated 10 times with different seeds.

| Models | Mean (°) | Median (°) | Max (°) | tRMSE |
|-----------------------|--------------------|--------------------|--------------------|--------------|
| KPConv [33] | 128.57 ± 0.97 | 123.22 ± 0.52 | 180.00 ± 0.00 | - |
| DGCNN + DCP-v1 [36] | 121.29 ± 0.90 | 137.19 ± 1.95 | 179.60 ± 0.00 | 0.081 |
| DGCNN + DCP-v2 [36] | 120.07 ± 1.28 | 132.54 ± 1.94 | 179.60 ± 0.00 | 0.072 |
| w/ SO(3) Aug | 121.61 ± 1.58 | 137.62 ± 1.85 | 179.60 ± 0.00 | 0.075 |
| EPN [4] | 1.62 ± 0.02 | 2.40 ± 0.08 | 110.14 ± 45.53 | - |
| E2PN [49] | 11.70 ± 0.25 | 13.71 ± 0.19 | 163.62 ± 15.70 | - |
| CSEConv [20] + DCP-v2 | 9.34 ± 0.16 | 2.93 ± 0.07 | 178.95 ± 1.06 | 0.17 |
| ECKConv + DCP-v2 | 0.63 ± 0.00 | 0.53 ± 0.00 | 8.57 ± 2.40 | 0.010 |

5.2. Pose Registration

Our pose registration model consisted of ECKConv local feature extractor and DCP method [36] to compute the relative pose between objects. Models experimented by Wang and Solomon [36] were compared as baselines since they utilize DGCNN [37] as a feature extractor. We also included models from Zhu et al. [49] and the CSEConv model sharing the identical architecture to ours as the equivariant baselines. Each metric represents the mean, median, maximum of error angles by rotations and RMSE of translation error. The training was conducted with randomly sampled poses from $SE(3)$ and the entire object categories.

Table 3 demonstrates the definite performance gap between our model and others in every metric. Baselines with DGCNN backbones could not handle the rotation difference sampled from the complete $SO(3)$ space. We also verified that applying $SO(3)$ augmentation on the source object during the training of DGCNN + DCP-v2 was unavailing either. Other baselines, only structurally equivariant to discrete group or $SO(3)$, were degraded by high maximum angle errors. ECKConv with the closest point approach fit best to the pose registration task thanks to its embedded and thorough symmetry to any $SE(3)$ actions.

5.3. Object Part Segmentation

Our part segmentation model adopted U-Net [31] inspired approach by Qi et al. [26] and adopted the feature interpolation module to up-sample the features of K-closest points. Please refer to Section 7.3 in the supplementary material for the interpolation details. We prepared PointNet++ [26], original DGCNN, model-agnostic methods based on DGCNN, and CSEConv baseline implemented with similar setups to ECKConv as baselines.

Table 4 shows that ECKConv achieved the instance averaged mIoUs over 83%, the best among the baselines when the $SO(3)$ is applied during the evaluation. The part class averaged mIoUs (mcIoUs) of ECKConv also reached comparable scores to the augmented and model-agnostic baselines. A qualitative analysis in Figure 4 revealed that CSE-

Table 4. Part segmentation on the ShapeNet. mIoU denotes the IoU per object averaged among every instance, and mcIoU denotes that IoUs are averaged per part class before the total mean.

| Models | I/I | | $I/SO(3)$ | | $SO(3)/SO(3)$ | |
|-----------------|--------------|--------------|--------------|--------------|---------------|--------------|
| | mIoU | mcIoU | mIoU | mcIoU | mIoU | mcIoU |
| PointNet++ [26] | 85.56 | 82.24 | 28.97 | 32.95 | 82.10 | 78.02 |
| DGCNN [37] | 85.13 | 85.41 | 31.48 | 32.19 | 77.60 | 78.24 |
| VN [9] | 81.74 | 82.06 | 81.73 | 82.05 | 81.76 | 82.10 |
| LC [19] | 81.04 | 81.43 | 81.07 | 81.45 | 81.05 | 81.53 |
| PRLC [22] | 79.38 | 79.90 | 79.39 | 79.91 | - | - |
| CSEConv [20] | 35.80 | 32.23 | 35.80 | 32.23 | 35.51 | 33.20 |
| ECKConv | 83.78 | 81.19 | 83.78 | 81.19 | 83.68 | 80.99 |

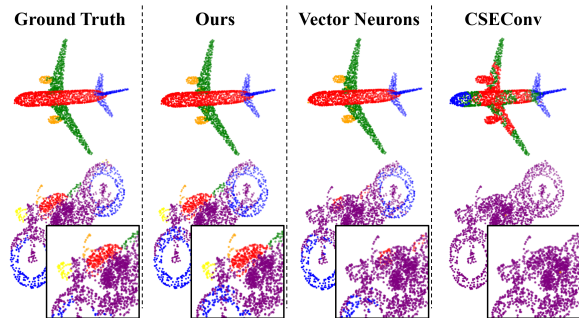


Figure 4. Visualization of the part segmentation in the ShapeNet by ECKConv (Ours), Vector Neurons [9], and CSEConv [20].

conv failed to discern local geometries even in the simple objects. Contrarily, ECKConv distinguished fine local features, e.g., the saddle and wheel of the bike, more accurately than other baselines. Unlike the previous experiments where learning the global shape was enough to solve the task, the performance gap in the segmentation task validates the outstanding capability of learning local geometries by ECKConv among the intertwiner convolution framework.

5.4. Indoor Semantic Segmentation

Our indoor segmentation model cropped $4 m^2$ square sub-regions and sampled the points from a single scene during its training due to the large scale of S3DIS, following previous researches [10, 32]. Similar to the part segmentation model, its U-Net architecture consisted of 30 layers of ECKConv and received point clouds with normal vectors but without colors. It was evaluated to cover the whole points of each aligned scene in the Area 5; we divided the scene to sub-regions with one meter strides, and every point in each region was split to uniformly sampled point clouds. We also voted 3 times to decide the final prediction as previous works [10, 32–34] and measured the segmentation performance with overall accuracy (OA), mean accuracy (mACC), and mean intersection over unit (mIoU).

We compared ECKConv to DGCNN and KPConv trained with $SO(3)$ augmentation and rotation invariant

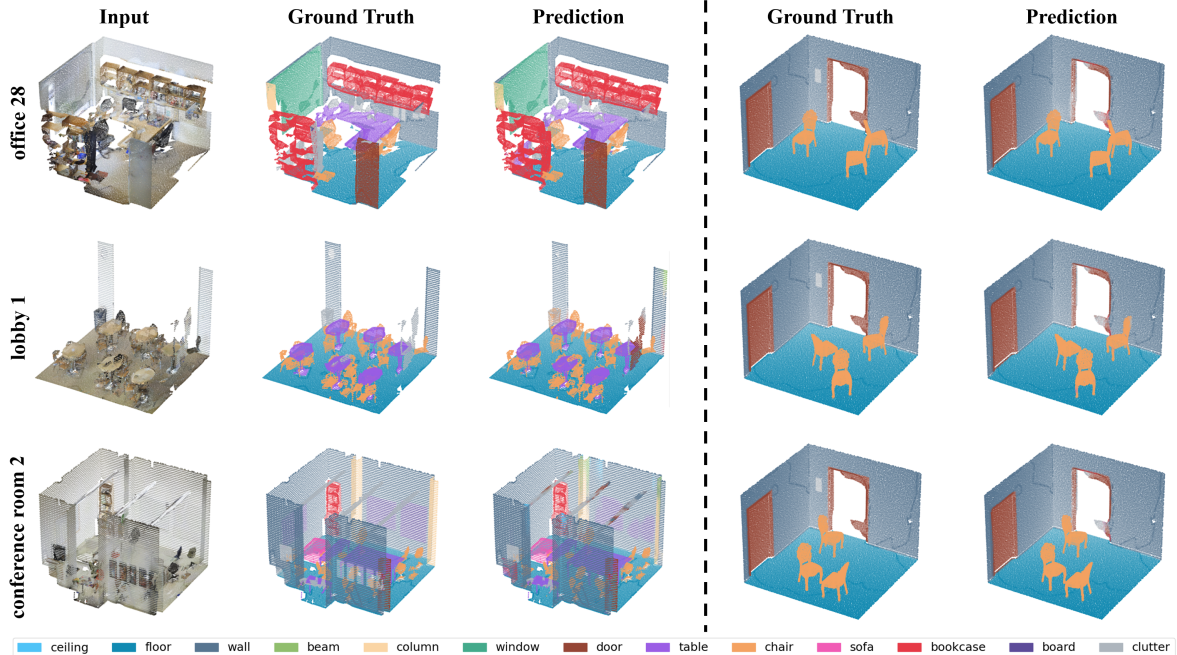


Figure 5. Semantic segmentation results by ECKConv on the Area 5 of S3DIS [1]. The ceiling and wall points that obscure the view point are omitted in the figures for the better visualization. (Left) The input, ground truth label, and prediction results of *office 28*, *lobby 1*, and *conference room 2* in the Area 5. Various indoor objects, *e.g.*, bookcase, table, chair, and sofa, are successfully segmented from the scenes by our method. (Right) The simulation by randomly placing chair objects from ModelNet40 [42] in the *hallway 8* of Area 5. Even though the chair objects are out-of-distribution from the S3DIS, our method segments every object from the simulated scenes.

Table 5. Semantic segmentation results on the Area 5 of S3DIS. † denotes the result reported in RI-MAE [32].

| Models | OA | mAcc | mIoU |
|--------------------------|--------------|--------------|--------------|
| DGCNN [37] w/ SO(3) Aug | 74.78 | 45.06 | 35.78 |
| KPConv [33] w/ SO(3) Aug | 84.50 | 64.66 | 57.42 |
| RIConv++ [44] | 84.68 | 66.41 | 56.94 |
| RI-MAE [32]† | - | - | 60.3 |
| ECKConv-Normal | 86.38 | 70.38 | 61.80 |

baselines, *e.g.*, RIConv++ [44] and RI-MAE [32]. Table 5 shows that the degradation by SO(3) augmentation was severe enough to drop the performance of non-equivariant methods lower than the rotation-invariant baselines; it necessitates the SE(3) symmetric model scalable enough to learn large-scale problems. Indeed, our ECKConv successfully conducted the segmentation as in the left of Figure 5 and reached the best performance in every metric, especially 61.80 in mIoU, which is the state-of-the-art performance among rotation-invariant methods in the S3DIS segmentation to the best of our knowledge.

We also conducted a simulation where chair objects from ModelNet40, out-of-distribution data to S3DIS, were randomly placed in the *hallway 8* of Area 5. As shown in the right of Figure 5, our method discerned the chairs regard-

less of their poses on the floor. Please refer to Figure 9 in the supplementary material for more qualitative simulation results. They verified that not only ECKConv is scalable enough but also its locally SE(3) equivariant features plays an essential role in resolving large-scale problems.

6. Conclusion

We propose ECKConv, SE(3) equivariant convolutional networks for point clouds using the intertwiner framework. We formalize the kernel domain as the double coset space of SE(3) acted by SO(2) subgroups and acquire the parameters defining SE(3)-invariant and disjoint orbits, guaranteeing the equivariance and injectiveness of the kernel domain. Utilizing the coordinate-based networks with the Gaussian embedding, the double coset parameters from the normalized receptive field in a ball shape of ECKConv are mapped to the weights for the basis kernel maps, enhancing the capability to learn local geometries. We also reformulate the explicit kernel computation and grant the memory scalability to ECKConv. Extensive experiments in the ModelNet40, ShapeNet, and S3DIS empirically validated the enhanced performance and efficiency of ECKConv, which achieved the best performance among the state-of-the-art equivariant or rotation-invariant point cloud methods in diverse synthetic and real-world problems.

Acknowledgement This work was partly supported by grants from the IITP (RS-2021-II211343-GSAI/10%, RS-2022-II220951-LBA/15%, RS-2022-II220953-PICA/15%), the NRF (RS-2024-00353991-SPARC/15%, RS-2023-00274280-HEI/15%), the KEIT (RS-2025-25453780/15%), and the KIAT (RS-2025-25460896/15%), funded by the Korean government.

References

- [1] Iro Armeni, Ozan Sener, Amir R Zamir, Helen Jiang, Ioannis Brilakis, Martin Fischer, and Silvio Savarese. 3d semantic parsing of large-scale indoor spaces. In *Proceedings of the IEEE conference on computer vision and pattern recognition*, pages 1534–1543, 2016. [2](#), [6](#), [8](#), [5](#)
- [2] Johann Brehmer, Sönke Behrends, Pim De Haan, and Taco Cohen. Does equivariance matter at scale? *Transactions on Machine Learning Research*, 2025. [1](#)
- [3] Angel X Chang, Thomas Funkhouser, Leonidas Guibas, Pat Hanrahan, Qixing Huang, Zimo Li, Silvio Savarese, Manolis Savva, Shuran Song, Hao Su, et al. Shapenet: An information-rich 3d model repository. *arXiv preprint arXiv:1512.03012*, 2015. [2](#), [6](#), [5](#)
- [4] Haiwei Chen, Shichen Liu, Weikai Chen, Hao Li, and Randall Hill. Equivariant point network for 3d point cloud analysis. In *Proceedings of the IEEE/CVF conference on computer vision and pattern recognition*, pages 14514–14523, 2021. [1](#), [2](#), [4](#), [6](#), [7](#)
- [5] Taco Cohen and Max Welling. Group equivariant convolutional networks. In *International conference on machine learning*, pages 2990–2999. PMLR, 2016. [1](#), [2](#), [3](#)
- [6] Taco S Cohen and Max Welling. Steerable cnns. *arXiv preprint arXiv:1612.08498*, 2016. [1](#), [2](#)
- [7] Taco S Cohen, Mario Geiger, and Maurice Weiler. Intertwiners between induced representations (with applications to the theory of equivariant neural networks). *arXiv preprint arXiv:1803.10743*, 2018. [2](#), [3](#)
- [8] Taco S Cohen, Mario Geiger, and Maurice Weiler. A general theory of equivariant cnns on homogeneous spaces. *Advances in neural information processing systems*, 32, 2019. [2](#), [3](#)
- [9] Congyue Deng, Or Litany, Yueqi Duan, Adrien Poulenard, Andrea Tagliasacchi, and Leonidas J Guibas. Vector neurons: A general framework for so (3)-equivariant networks. In *Proceedings of the IEEE/CVF International Conference on Computer Vision*, pages 12200–12209, 2021. [2](#), [3](#), [6](#), [7](#)
- [10] Runpei Dong, Zekun Qi, Linfeng Zhang, Junbo Zhang, Jianjian Sun, Zheng Ge, Li Yi, and Kaisheng Ma. Autoencoders as cross-modal teachers: Can pretrained 2d image transformers help 3d representation learning? *arXiv preprint arXiv:2212.08320*, 2022. [7](#), [2](#)
- [11] Jiajun Fei and Zhidong Deng. Rotation invariance and equivariance in 3d deep learning: a survey. *Artificial Intelligence Review*, 57(7):168, 2024. [1](#)
- [12] Marc Finzi, Samuel Stanton, Pavel Izmailov, and Andrew Gordon Wilson. Generalizing convolutional neural networks for equivariance to lie groups on arbitrary continuous data. In *International conference on machine learning*, pages 3165–3176. PMLR, 2020. [1](#)
- [13] Fabian Fuchs, Daniel Worrall, Volker Fischer, and Max Welling. Se (3)-transformers: 3d roto-translation equivariant attention networks. *Advances in neural information processing systems*, 33:1970–1981, 2020. [2](#), [6](#)
- [14] Jan Gerken, Oscar Carlsson, Hampus Linander, Fredrik Ohlsson, Christoffer Petersson, and Daniel Persson. Equivariance versus augmentation for spherical images. In *International Conference on Machine Learning*, pages 7404–7421. PMLR, 2022. [1](#)
- [15] Meng-Hao Guo, Jun-Xiong Cai, Zheng-Ning Liu, Tai-Jiang Mu, Ralph R Martin, and Shi-Min Hu. Pct: Point cloud transformer. *Computational Visual Media*, 7:187–199, 2021. [2](#), [6](#)
- [16] Yulan Guo, Hanyun Wang, Qingyong Hu, Hao Liu, Li Liu, and Mohammed Bennamoun. Deep learning for 3d point clouds: A survey. *IEEE transactions on pattern analysis and machine intelligence*, 43(12):4338–4364, 2020. [1](#)
- [17] Kaiming He, Xiangyu Zhang, Shaoqing Ren, and Jian Sun. Deep residual learning for image recognition. In *Proceedings of the IEEE conference on computer vision and pattern recognition*, pages 770–778, 2016. [6](#)
- [18] Anastasia Ioannidou, Elisavet Chatzilari, Spiros Nikolopoulos, and Ioannis Kompatsiaris. Deep learning advances in computer vision with 3d data: A survey. *ACM computing surveys (CSUR)*, 50(2):1–38, 2017. [1](#)
- [19] Sékou-Oumar Kaba, Arnab Kumar Mondal, Yan Zhang, Yoshua Bengio, and Siamak Ravanbakhsh. Equivariance with learned canonicalization functions. In *International Conference on Machine Learning*, pages 15546–15566. PMLR, 2023. [3](#), [6](#), [7](#)
- [20] Jaemin Kim, Hee Bin Yoo, Dong-Sig Han, Yeon-Ji Song, and Byoung-Tak Zhang. Continuous so (3) equivariant convolution for 3d point cloud analysis. In *European Conference on Computer Vision*, pages 59–75. Springer, 2024. [2](#), [3](#), [4](#), [5](#), [6](#), [7](#)
- [21] Yangyan Li, Rui Bu, Mingchao Sun, Wei Wu, Xinhan Di, and Baoquan Chen. Pointcnn: Convolution on x-transformed points. *Advances in neural information processing systems*, 31, 2018. [2](#)
- [22] Arnab Kumar Mondal, Siba Smarak Panigrahi, Oumar Kaba, Sai Rajeswar Mudumba, and Siamak Ravanbakhsh. Equivariant adaptation of large pretrained models. *Advances in Neural Information Processing Systems*, 36:50293–50309, 2023. [3](#), [6](#), [7](#), [2](#)
- [23] Philip Müller, Vladimir Golkov, Valentina Tomassini, and Daniel Cremers. Rotation-equivariant deep learning for diffusion mri. *arXiv preprint arXiv:2102.06942*, 2021. [1](#)
- [24] Omri Puny, Matan Atzmon, Heli Ben-Hamu, Ishan Misra, Aditya Grover, Edward J Smith, and Yaron Lipman. Frame averaging for invariant and equivariant network design. In *10th International Conference on Learning Representations, ICLR 2022*, 2022. [3](#), [6](#)
- [25] Charles R Qi, Hao Su, Kaichun Mo, and Leonidas J Guibas. Pointnet: Deep learning on point sets for 3d classification and segmentation. In *Proceedings of the IEEE conference*

- on computer vision and pattern recognition, pages 652–660, 2017. 2
- [26] Charles Ruizhongtai Qi, Li Yi, Hao Su, and Leonidas J Guibas. Pointnet++: Deep hierarchical feature learning on point sets in a metric space. *Advances in neural information processing systems*, 30, 2017. 2, 4, 5, 6, 7, 1
- [27] Ali Rahimi and Benjamin Recht. Random features for large-scale kernel machines. *Advances in neural information processing systems*, 20, 2007. 3
- [28] Nikhila Ravi, Jeremy Reizenstein, David Novotny, Taylor Gordon, Wan-Yen Lo, Justin Johnson, and Georgia Gkioxari. Accelerating 3d deep learning with pytorch3d. *arXiv preprint arXiv:2007.08501*, 2020. 1
- [29] David W Romero, Robert-Jan Bruintjes, Jakub M Tomczak, Erik J Bekkers, Mark Hoogendoorn, and Jan C van Gemert. Flexconv: Continuous kernel convolutions with differentiable kernel sizes. *arXiv preprint arXiv:2110.08059*, 2021. 2
- [30] David W Romero, Anna Kuzina, Erik J Bekkers, Jakub M Tomczak, and Mark Hoogendoorn. Ckconv: Continuous kernel convolution for sequential data. *arXiv preprint arXiv:2102.02611*, 2021. 2
- [31] Olaf Ronneberger, Philipp Fischer, and Thomas Brox. U-net: Convolutional networks for biomedical image segmentation. In *Medical image computing and computer-assisted intervention—MICCAI 2015: 18th international conference, Munich, Germany, October 5–9, 2015, proceedings, part III 18*, pages 234–241. Springer, 2015. 7, 5
- [32] Kunming Su, Qiuxia Wu, Panpan Cai, Xiaogang Zhu, Xuequan Lu, Zhiyong Wang, and Kun Hu. Ri-mae: Rotation-invariant masked autoencoders for self-supervised point cloud representation learning. In *Proceedings of the AAAI Conference on Artificial Intelligence*, pages 7015–7023, 2025. 3, 6, 7, 8, 2
- [33] Hugues Thomas, Charles R Qi, Jean-Emmanuel Deschaud, Beatriz Marcotequi, François Goulette, and Leonidas J Guibas. Kpconv: Flexible and deformable convolution for point clouds. In *Proceedings of the IEEE/CVF international conference on computer vision*, pages 6411–6420, 2019. 2, 4, 6, 7, 8
- [34] Hugues Thomas, Yao-Hung Hubert Tsai, Timothy D Barfoot, and Jian Zhang. Kpconvx: Modernizing kernel point convolution with kernel attention. In *Proceedings of the IEEE/CVF Conference on Computer Vision and Pattern Recognition*, pages 5525–5535, 2024. 4, 6, 7
- [35] Nathaniel Thomas, Tess Smidt, Steven Kearnes, Lusann Yang, Li Li, Kai Kohlhoff, and Patrick Riley. Tensor field networks: Rotation-and translation-equivariant neural networks for 3d point clouds. *arXiv preprint arXiv:1802.08219*, 2018. 2, 6
- [36] Yue Wang and Justin M Solomon. Deep closest point: Learning representations for point cloud registration. In *Proceedings of the IEEE/CVF international conference on computer vision*, pages 3523–3532, 2019. 7, 2
- [37] Yue Wang, Yongbin Sun, Ziwei Liu, Sanjay E Sarma, Michael M Bronstein, and Justin M Solomon. Dynamic graph cnn for learning on point clouds. *ACM Transactions on Graphics (tog)*, 38(5):1–12, 2019. 2, 6, 7, 8
- [38] Lisa Weijler and Pedro Hermosilla. Efficient continuous group convolutions for local se (3) equivariance in 3d point clouds. *arXiv preprint arXiv:2502.07505*, 2025. 2
- [39] Wenxuan Wu, Zhongang Qi, and Li Fuxin. Pointconv: Deep convolutional networks on 3d point clouds. In *Proceedings of the IEEE/CVF Conference on computer vision and pattern recognition*, pages 9621–9630, 2019. 2, 5, 6
- [40] Xiaoyang Wu, Yixing Lao, Li Jiang, Xihui Liu, and Hengshuang Zhao. Point transformer v2: Grouped vector attention and partition-based pooling. *Advances in Neural Information Processing Systems*, 35:33330–33342, 2022. 2
- [41] Xiaoyang Wu, Li Jiang, Peng-Shuai Wang, Zhijian Liu, Xihui Liu, Yu Qiao, Wanli Ouyang, Tong He, and Hengshuang Zhao. Point transformer v3: Simpler faster stronger. In *Proceedings of the IEEE/CVF Conference on Computer Vision and Pattern Recognition*, pages 4840–4851, 2024. 2, 6
- [42] Zhirong Wu, Shuran Song, Aditya Khosla, Fisher Yu, Linguang Zhang, Xiaoou Tang, and Jianxiong Xiao. 3d shapenets: A deep representation for volumetric shapes. In *Proceedings of the IEEE conference on computer vision and pattern recognition*, pages 1912–1920, 2015. 1, 2, 4, 6, 8
- [43] Zhiyuan Zhang, Binh-Son Hua, David W Rosen, and Sai-Kit Yeung. Rotation invariant convolutions for 3d point clouds deep learning. In *2019 International conference on 3d vision (3DV)*, pages 204–213. IEEE, 2019. 3
- [44] Zhiyuan Zhang, Binh-Son Hua, and Sai-Kit Yeung. Riconv++: Effective rotation invariant convolutions for 3d point clouds deep learning. *arXiv preprint arXiv:2202.13094*, 2022. 3, 8, 2
- [45] Hengshuang Zhao, Li Jiang, Jiaya Jia, Philip HS Torr, and Vladlen Koltun. Point transformer. In *Proceedings of the IEEE/CVF international conference on computer vision*, pages 16259–16268, 2021. 2
- [46] Maksim Zhdanov, Nico Hoffmann, and Gabriele Cesa. Implicit convolutional kernels for steerable cnns. *Advances in Neural Information Processing Systems*, 36, 2024. 2
- [47] Jianqiao Zheng, Sameera Ramasinghe, and Simon Lucey. Rethinking positional encoding. *arXiv preprint arXiv:2107.02561*, 2021. 4, 5
- [48] Jianqiao Zheng, Sameera Ramasinghe, Xueqian Li, and Simon Lucey. Trading positional complexity vs deepness in coordinate networks. In *European Conference on Computer Vision*, pages 144–160. Springer, 2022. 4, 5
- [49] Minghan Zhu, Maani Ghaffari, William A Clark, and Hui Peng. E2pn: Efficient se (3)-equivariant point network. In *Proceedings of the IEEE/CVF Conference on Computer Vision and Pattern Recognition*, pages 1223–1232, 2023. 1, 2, 3, 4, 6, 7

Learning Coordinate-based Convolutional Kernels for Continuous SE(3) Equivariant and Efficient Point Cloud Analysis

Supplementary Material

Algorithm 1 The coset augmentation from the coordinates

Input: coordinates set $\mathbf{X} \in \mathbb{R}^{N \times 3}$, neighborhood size K
Output: augmented cosets $\mathbf{N} \in \mathbb{R}^{N \times 3}$, s.t. $\mathbf{N} \subset S^2$

- 1: $\{\mathbf{x}^n, \{\mathbf{x}_i^n\}_{i=1}^K\}_{n=1}^N \leftarrow \text{K-NN}(\mathbf{X}, \mathbf{X}; K)$
- 2: **for** $n = 1$ to N **do**
- 3: $\{\mathbf{n}_1^n, \dots, \mathbf{n}_K^n\} \leftarrow \{\mathbf{x}_1^n - \mathbf{x}^n, \dots, \mathbf{x}_K^n - \mathbf{x}^n\}$
- 4: $\mathbf{n}^n \leftarrow \frac{1}{K} \sum_i \mathbf{n}_i^n$
- 5: **if** $\|\mathbf{n}^n\|_2 > 1e-5$ **then**
- 6: $\hat{\mathbf{n}}^n \leftarrow \frac{\mathbf{n}^n}{\|\mathbf{n}^n\|_2}$
- 7: **else**
- 8: $\hat{\mathbf{n}}^n \leftarrow$ the least eigenvector of $\text{PCA}(\{\mathbf{n}_i^n\}_{i=1}^K)$
- 9: **end if**
- 10: **end for**
- 11: $\mathbf{N} \leftarrow [\hat{\mathbf{n}}^1, \dots, \hat{\mathbf{n}}^N]^\top$
- 12: **return** \mathbf{N}

7. Model Architectures and Training Setups

We explain the details of ECKConv implementation and enumerate the training configurations of our models. Every ECKConv model is conducted on a single RTX 3090 GPU. Their architectures are illustrated in Figures 7a, 7b, 8a and 8b. When applying neighboring algorithms specified for point clouds, e.g., farthest point sampling, k-nearest neighbors, ball query, and PCA among point groups, we utilized the implementations from PyTorch3D [28].

7.1. Details of ECKConv Block

This section delineates the detailed computation of ECKConv block, which is also illustrated in Figure 6. Given the input point cloud $\{(x^n, f^n) | x^n = (\mathbf{x}^n, \mathbf{n}^n), f^n = f(x^n)\}_{n=1}^N$, the centroids for convolution $\{(x^m, f^m)\}_{m=1}^M$, where $M \leq N$, are sampled first by farthest point sampling [26] using the coordinate \mathbf{x}^m s. Then, a ball query groups the local neighbors with maximal k neighbors $\mathcal{N}(x^m) = \{x_i^m | x_i^m = (\mathbf{x}_i^m, \mathbf{n}_i^m)\}_{i=1}^k$ from the input points for each centroid x^m . It gathers features in $\{f^n\}_{n=1}^N$ into $\{\{f_i^m\}_{i=1}^k\}_{m=1}^M$ by every $\mathcal{N}(x^m)$, and the ECKConv layer operates on every neighborhood and its gathered feature, yielding the output features $\{(f * \kappa)^m\}_{m=1}^M$. After the block, batch normalization and GELU activation are applied on the $\{(f * \kappa)^m\}_{m=1}^M$, and the pair of $\{(x^m, (f * \kappa)^m)\}_{m=1}^M$ is propagated as a new point cloud towards the next layer. The above process is summarized in Algorithm 2.

Algorithm 2 The process of ECKConv block

Input: coordinates $\mathcal{X}_{\text{in}} \in \mathbb{R}^{N \times 6}$, features $\mathcal{F}_{\text{in}} \in \mathbb{R}^{N \times C_{\text{in}}}$
Output: $\{x^m\}_{m=1}^M, \{f^n\}_{n=1}^N$

- 1: $\{x^n\}_{n=1}^N \leftarrow \mathcal{X}_{\text{in}}; \{f^n\}_{n=1}^N \leftarrow \mathcal{F}_{\text{in}}$
- 2: $\{x^m\}_{m=1}^M \leftarrow$ farthest-point-sampling($\{x^n\}_{n=1}^N, M$)
- 3: **Gather** $\{f^m\}_{m=1}^M$ for $\{x^m\}_{m=1}^M$
- 4: $\mathcal{X}_{\text{cnt}} \leftarrow \{x^m\}_{m=1}^M, \mathcal{F}_{\text{cnt}} \leftarrow \{f^m\}_{m=1}^M$
- 5: $\{\mathcal{N}(x^m)\}_{m=1}^M \leftarrow$ ball-query($\{x^m\}_{m=1}^M, \{x^n\}_{n=1}^N, k$)
- 6: **Gather** $\{\{f_i^m\}_{i=1}^k\}_{m=1}^M$ for $\{\mathcal{N}(x^m)\}_{m=1}^M$
- 7: $\{(f * \kappa)^m\}_{m=1}^M \leftarrow$ ECKConv($\{x^m\}_{m=1}^M, \{\mathcal{N}(x^m)\}_{m=1}^M, \{\{f_i^m\}_{i=1}^k\}_{m=1}^M$)
- 8: $\mathcal{F}_{\text{conv}} \leftarrow \{(f * \kappa)^m\}_{m=1}^M$
- 9: **return** $\mathcal{X}_{\text{cnt}}, \mathcal{F}_{\text{cnt}}, \mathcal{F}_{\text{conv}}$
 $\triangleright \mathcal{F}_{\text{cnt}}$ is utilized only in the residual connection

7.2. Coset Augmentation of Point Clouds

If the ground truth normal vector were not given in the inputs, we heuristically lift the 3D coordinate to the coset in S^2 as Algorithm 1. It averages every difference between the neighbor points and the centroid and normalize the average into a unit vector unless its norm is not too small. If it is, it exploits PCA on the neighbors to estimate the normal vector for the centroid. We also experimented exploiting only the normal vectors estimated by PCA before the ECKConv layers, but Algorithm 1 empirically performed better in the ModelNet40 experiments. We applied this to every our models except ECKConv-Normal in the ModelNet40 classification and the S3DIS segmentation experiments.

7.3. Point Feature Propagation Module

We adopt this module suggested by Qi et al. [26] in our segmentation models, up-sampling point features from a coarse point cloud $\mathcal{X}' \in \mathbb{R}^{M \times 3}$ onto a fine one $\mathcal{X} \in \mathbb{R}^{N \times 3}$ such that $N > M$. Querying the top-K nearest points from the coarse point cloud per each fine point, local features from queried points are gathered with normalized weights reciprocal to distances and concatenated to features of the query point:

$$f_i^{\text{FP}} = \frac{\sum_{k=1}^K w_{ik} f'_{ik}}{\sum_{k=1}^K w_{ik}}, \quad w_{ik} = \frac{1}{\|x_i - x'_{ik}\|_2^2}, \quad (13)$$

where $x_i \in \mathcal{X}$, and $x'_{ik} \in \mathcal{X}'$ is queried to x_i by KNN with corresponding feature f'_{ik} . Then the upsampled feature f_i^{FP} is concatenated to f_i , the feature of x_i before the feature

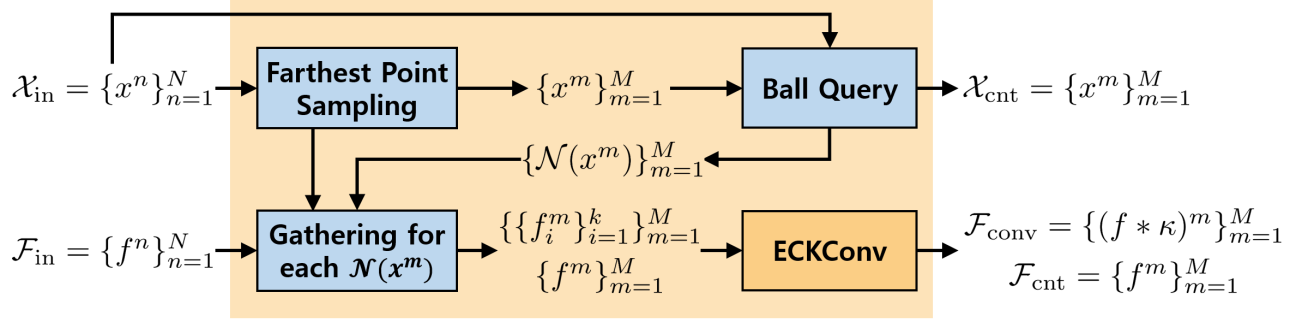


Figure 6. Detailed architectures of ECKConv block. We substitute abstract variables from Figure 3 with actual computational variables.

propagation, and the module propagates a new point feature set $\{[f_i, f_i^{\text{FP}}]\}_{i=1}^N$ to the following ECKConv layer. We set $K = 1$ and $K = 3$ for object part and indoor semantic segmentation model each.

7.4. Training Configurations

7.4.1. ModelNet40 Classification

We let every baseline training follow its original configuration of training: the number of input points, whether to utilize a normal vector, augmentation except SO(3) rotation, and other optimizer hyperparameters. For our method, we sampled 1024 points for each point cloud and applied the scaling augmentation during the training, *i.e.*, the scales of the object in XYZ directions were randomly rescaled in range $(\frac{2}{3}, 1.5)$. Each minibatch contained 16 point clouds, and its cross entropy loss was smoothed with parameter 0.2 and minimized by Adam optimizer, whose initial learning rate was $1e-4$ and scheduled to $1e-6$ by cosine annealing scheduler during 200 epochs.

7.4.2. ModelNet40 Pose Registration

Our ECKConv layers extracted local features from the two distinct inputs, named the source and target. We adopted Deep Closest Point [36] to determine the proper interpolation value of source coordinates that match the target coordinates. A variant of the transformer encoder-decoder structure plays a critical role in DCP to find the interpolation score between points. Every deep learning module here shares its parameters for both source and target. Finally, the relative pose $\mathbf{T}_{\text{pred}} = (\mathbf{R}_{\text{pred}}, \mathbf{t}_{\text{pred}})$ from the source to target can be readily computed by applying the singular value decomposition and mean difference. Following Wang and Solomon [36], the following loss was minimized:

$$\mathcal{L}(\mathbf{T}_{\text{pred}}, \mathbf{T}_{\text{gt}}) = \|\mathbf{R}_{\text{pred}} \mathbf{R}_{\text{gt}}^\top - \mathbf{I}\|_2^2 + \|\mathbf{t}_{\text{pred}} - \mathbf{t}_{\text{gt}}\|_2^2. \quad (14)$$

The training was conducted for 50 epochs, and each minibatch contains 16 pairs without augmentation. Adam optimizer minimizes the loss with $1e-4$ initial learning rate scheduled to $1e-6$ by cosine annealing scheduler.

7.4.3. ShapeNet Part Segmentation

We configured the number of points in a point cloud to 2048 in every model for fair comparison, since the number of samples in a point cloud affects the IoU metrics. It might influence the performance discrepancy of PRLC [22] between its reported result and our experiment, whose number of points is 1024 in its original implementation. We applied an identical augmentation protocol from our classification model training. A cross-entropy loss was computed on every point of each input and smoothed with parameter 0.2. The loss on minibatch containing 16 point clouds was minimized by Adam optimizer with hyperparameter $\beta_1 = 0.5$, and its initial learning rate was scheduled from $1e-4$ to $1e-6$ by the cosine annealing during 250 epochs.

7.4.4. S3DIS Semantic Segmentation

As stated in Section 5.4, we adopted the training protocols by Dong et al. [10], Su et al. [32], Zhang et al. [44] to crop a $4m^2$ region and sample 4096 points within it. A single room in the area was resampled multiple times in a single epoch to cover its whole scene with the cropped regions. The cropped regions were randomly scaled in range $(\frac{2}{3}, 1.5)$ along the XY directions and flipped along the X-axis with probability 0.5 during the training. Besides, the label weight for cross-entropy loss was precomputed since the imbalance among the semantic category is severe in the S3DIS. The cross entropy loss was minimized by Adam optimizer with learning rate $1e-4$ during 80 epochs.

8. Setups for CSEConv Baselines

Since CSEConv [20] is our main baseline with respect to the scalability, we detail the setups for CSEConv baselines in the pose registration and part segmentation, which were not experimented in its original paper. Every CSEConv baseline followed the initial feature generation protocol suggested by Kim et al. [20].

Table 6. Memory and time costs during the training, compared between ECKConv and CSEConv baselines from the pose registration and part segmentation tasks.

| | Models | Memory (GB) ↓ | #Batch/sec ↑ | batch size | #params |
|----------|---------|---------------|--------------|------------|---------|
| pose reg | CSEConv | 39.09 | 3.37 | 16 | 10.8M |
| | ECKConv | 5.37 | 7.39 | 16 | 4.1M |
| part seg | CSEConv | 66.46 | 2.04 | 6 | 14.9M |
| | ECKConv | 10.26 | 3.80 | 16 | 22.5M |

8.1. Pose Registration

As stated in the main paper, it shared the identical model and training configurations to the ECKConv model, e.g., the basis dimension of coordinate-based networks (though CSEConv uses random Fourier feature [27]), the number of layers, the dimension of each hidden layer, the cardinality of neighbors per layer, and training hyperparameters. However, 6 GPUs were required to train this model in our workstation. It shifted both source and target point clouds to the origin by subtracting geometric means since CSEConv only preserves SO(3) symmetry. After the extraction, the model replaced down-sampled point clouds to the original center coordinates before DCP method.

8.2. Part Segmentation

Our CSEConv baseline also followed U-Net style architecture but had only three down-sampling and up-sampling layers each. It shared the identical training hyperparameters to the ECKConv experiment except for the batch size and training epochs, which reduced to 6 point clouds and 100 epochs. This configuration also utilized 6 GPUs for the training in our workstation.

8.3. Scalability Comparisons

We additionally measure the cost of CSEConv baselines during the training and compare them with our models in Table 6. Since the training setups which affected their efficiency varied among experiments, their batch and parameter sizes are reported as well.

We observed the consistency in their training efficiency, which matches the scalability statement in Proposition 4.1. When models shared the identical architecture as the pose registration task, ECKConv was more efficient than CSEConv both in memory and time costs. Our method also consumed fewer resources than CSEConv while processing more parameters and inputs in the part segmentation experiment. These results supplement the scalability of ECKConv, which effectively exploits computation resources and is scalable to obtain sufficient model capacity.

Table 7. Ablation experiments on the hyperparameters of ECKConv in the ModelNet40 classification task, where models received randomly rotated inputs only during the evaluation ($I/SO(3)$). Default values are $A = 22$, $\Psi \in \mathbb{R}^{64}$, and $K = 32$.

| Ablation Studies | #Anchor Bases | | Gau(-) Bandwidth | | #Neighbors for Alg 1. | |
|------------------|---------------|----------|-------------------------|-----------------------------|-----------------------|-----------|
| | $A = 1$ | $A = 64$ | $\Psi \in \mathbb{R}^4$ | $\Psi \in \mathbb{R}^{256}$ | $K = 8$ | $K = 128$ |
| Acc (%) | 89.22 | 90.19 | 88.86 | 90.32 | 90.32 | 89.95 |
| Mem (GB) ↓ | 4.36 | 6.57 | 1.90 | 14.51 | 4.90 | 4.90 |
| #Batch/sec ↑ | 10.20 | 5.62 | 10.65 | 2.69 | 7.58 | 6.83 |

9. Ablations on Hyperparameter Sensitivity

As the kernel structure and the coordinate lifting to coset space of ECKConv have diverse hyperparameters, we conducted ablation experiments in the ModelNet40 classification task to verify the sensitivity of ECKConv against such hyperparameters. The experiments varied the number of anchor bases (A), the bandwidth of Gaussian embedding (Ψ), and the number of neighbors during the coset lifting in Algorithm 1 (K) to extreme values. Table 7 demonstrates that the efficiencies of the variants were affected significantly when the hyperparameters related to the kernel (A , Ψ) varied, but their performances remained relatively robust. We conjecture that linear layers from skip connections in our method help maintain their performances.

10. Discussion on the Limitations

Although ECKConv proposes an SE(3)-symmetric and scalable convolution applicable to large-scale point cloud problems, its kernel is isotropic to SE(3) actions due to the utilization of the double coset element, which is composed of coset elements grouped by left actions of SO(2), and the confinement to scalar-type features. These factors decrease the directional expressivity of ECKConv to certain types of point cloud tasks where the point feature should be anisotropic, e.g., normal estimation, molecule structure prediction, and n-body problems. Expanding the resolvable domain of ECKConv would be an important future research direction that balances our scalable architecture with the inefficient yet expressive kernel designs from the previous steerable convolution studies.

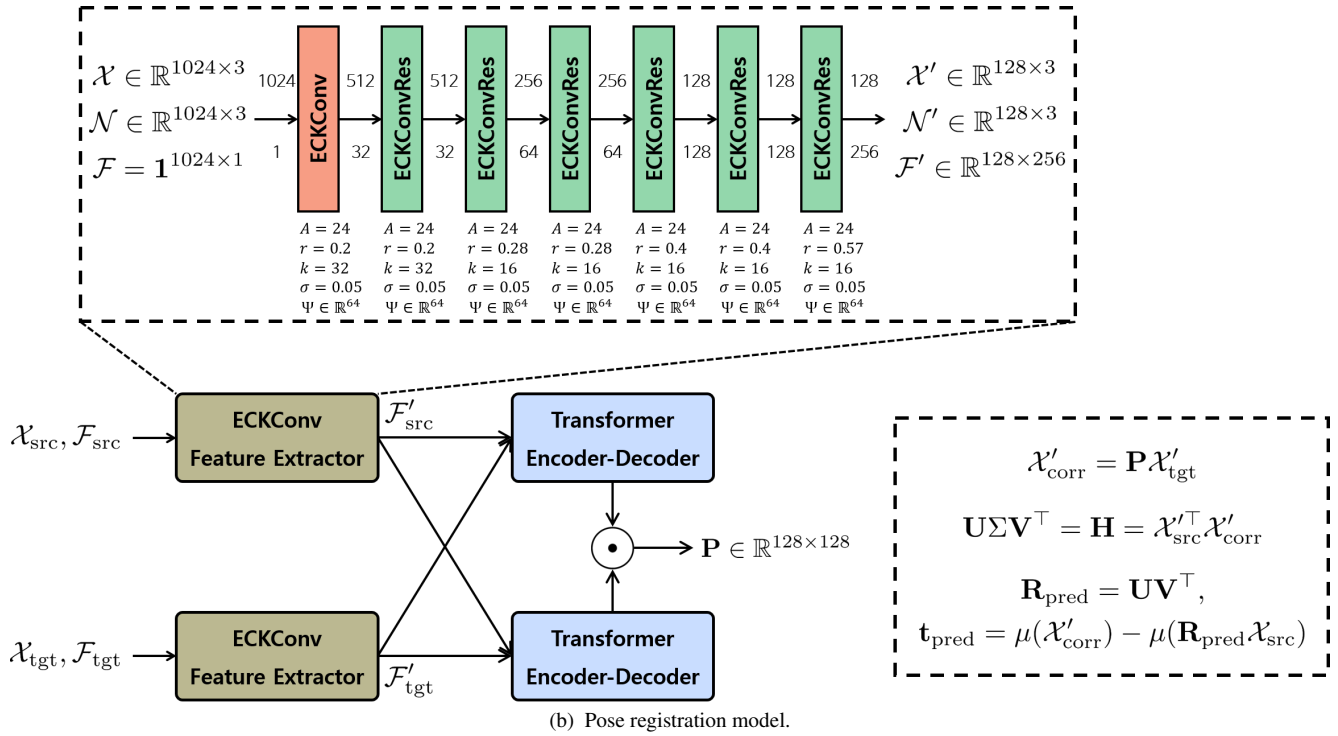
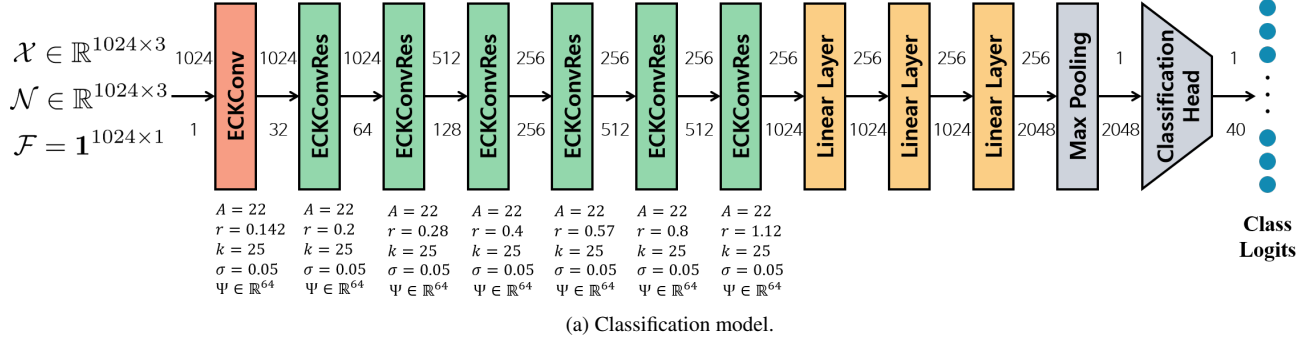
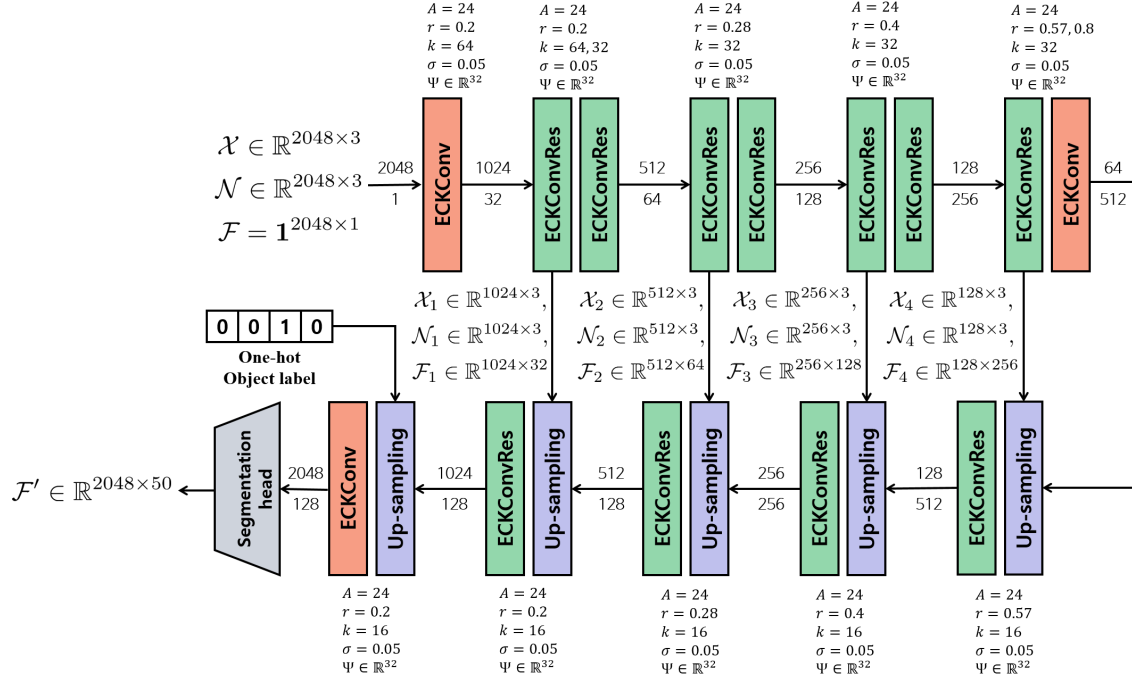
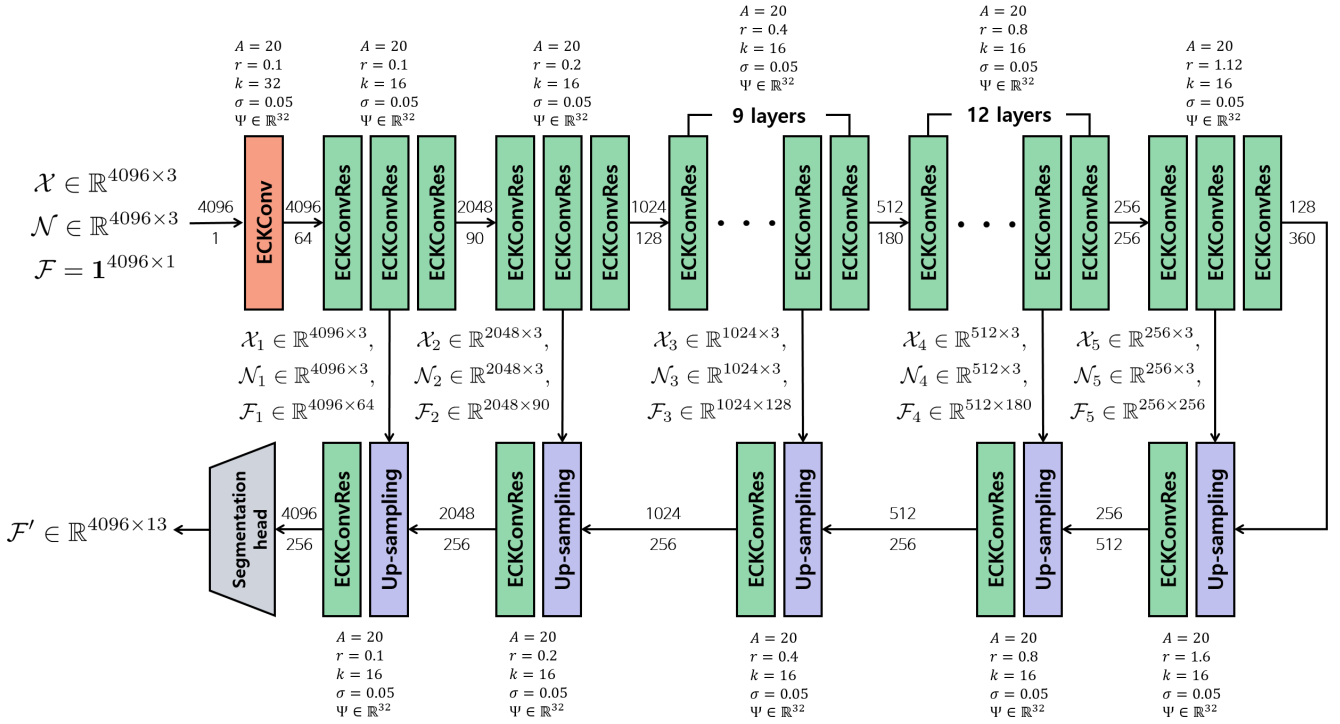


Figure 7. Architectures of ECKCov models for ModelNet40 [42] experiments. Since point clouds only contain 3D coordinates, we initialize its point feature as one vector per every point. An arrow between ECKConv layers designates the number of points and the dimension of each feature on its above and below. We also specify ECKConv hyperparameters below, such as the number of anchor points (A), a ball query radius (r), the maximal number of sampled points (k), the standard deviation of Gaussian kernel (σ), and the basis dimension of Gaussian embedding (Ψ) [47, 48]. Linear layers map every point feature with weight-sharing networks, and we omit batch normalization and activation next to these layers in the above figures.



(a) Part segmentation model for ShapeNet [3].



(b) Semantic segmentation model for S3DIS [1].

Figure 8. Architectures of ECKConv models for segmentation tasks in the ShapeNet and S3DIS. We applied U-Net [31] style architecture and up-sampled point features using Point Feature Propagation [26] module, which assigns coarse point features to its top-K closest neighbors skipped from previous layers, weighted by the reciprocal of the point distance in the coordinate space.

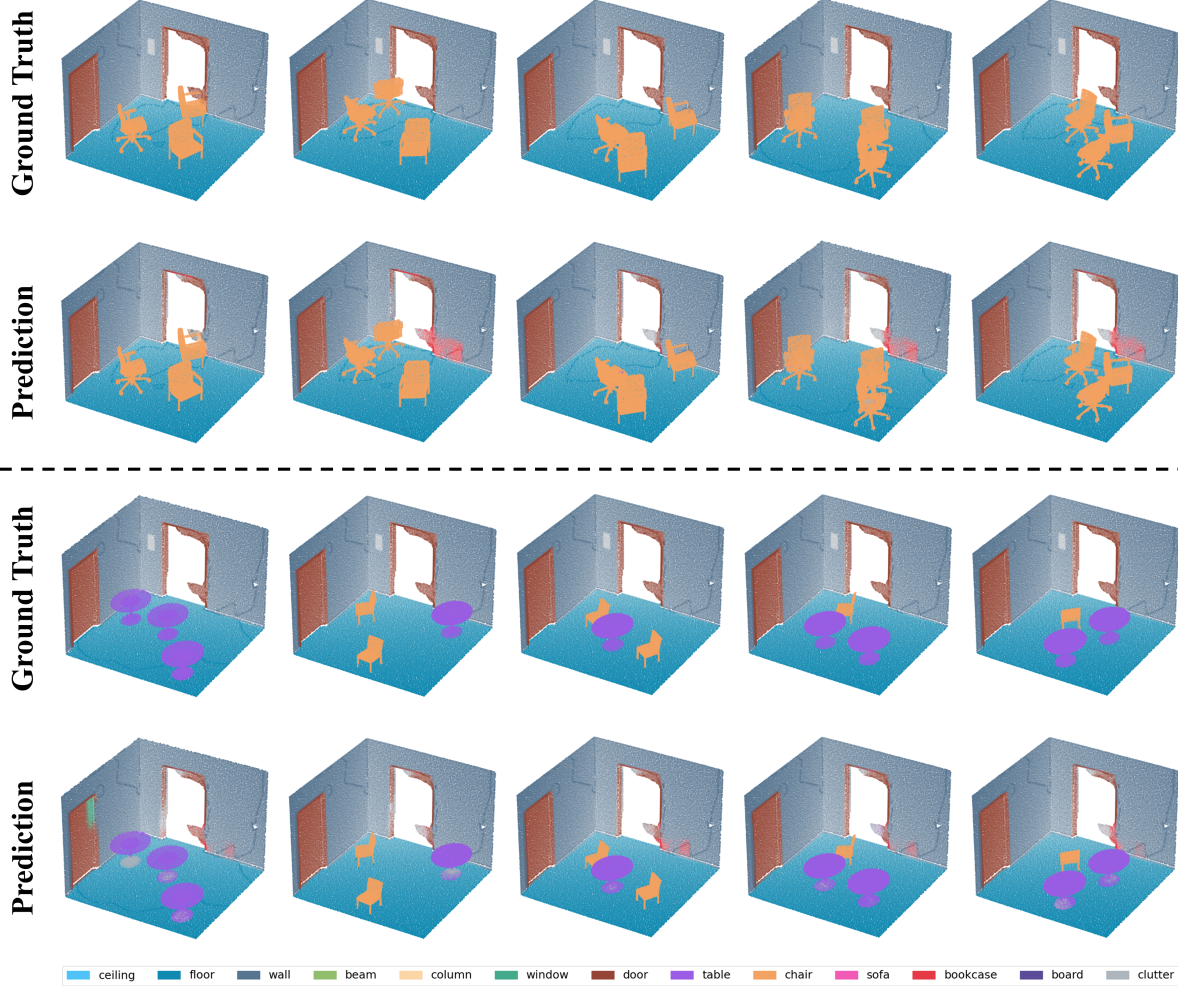


Figure 9. Qualitative results in S3DIS simulation experiments. (top) We diversified the objects from the chair category of ModelNet40. Our model consistently succeeded to discern chair objects with different shapes and poses. (bottom) We diversified the object category, adding the table object from ModelNet40. Our model showed consistent results on segmenting the table objects regardless of their numbers or poses, although noisy results on the bottom part of tables were also observed.